ADVANCED ENERGY MATERIALS
www.advenergymat.de

Sea State Adaptation Enhances Power Output of Triboelectric Nanogenerators for Tailored Ocean Wave Energy Harvesting

Isabel Gonçalves, Cátia Rodrigues, and João Ventura**

To face the climate crisis, sustainable energy harvesting systems are critical. Triboelectric nanogenerators (TENGs) are in the spotlight for their inexpensive and non-toxic manufacturing, allied with their excellence in harvesting low frequency vibrations. Ocean waves are a prime example of energy source in this regime, and their successful harvesting with TENGs has been widely demonstrated. However, the influence of wave characteristics on the power output of these devices has so far been overlooked. Here, the existence of a moving element that acts upon the nanogenerators is explored both with multiphysics simulations and an extensive experimental characterization under different operating conditions. It is shown how different sea states modulate the moving body velocity, and how the generator can be optimized to harvest waves with specific characteristics. In parallel, it is demonstrated that the power output is proportional to the contacting triboelectric layers velocity. Optimizing the dynamics of the moving body provides an efficient path to intentionally tune the contacting triboelectric layers velocity, and therefore improve the output of TENGs and their suitability to harvest specific sea states.

1. Introduction

Energy is the crucial resource of the modern world. However, we are still to find a balanced way to supply the world's energy needs without compromising our future.[1] To face the climate crisis, the adoption of sustainable energy harvesting technologies is a pressing need, where both the renewability of the energy source and the proximity of production and consumption sites are important factors.[2,3] From the different energy sources available, one of the most atractive is ocean wave energy. The oceans cover more than two thirds of the Earth's surface, with potential and kinetic energies, from waves alone, estimated at 32000 TWh/year,[4,5] surpassing the ≈ 28000 TWh of electricity consumed globally in 2022.[6]

In recent years, triboelectric nanogenerators (TENGs) have been shown to be exceptional fits to harvest this immense energy resource, due to their high efficiency in converting low frequency inputs into electrical energy.[7–10] TENGs take advantage of contact electrification and operate on the basis of electrostatic induction, converting mechanical into electrical energy.[11,12] Furthermore, thanks to their low fabrication cost and light weight, TENGs can be easily encapsulated and integrated inside wave energy converters (WECs) or regular ocean buoys.[13–15]

The most common TENG prototypes proposed for ocean wave energy harvesting involve a moving element, such as a pendulum,[16–22] a bar[23–25] or a sphere.[26–34] For instance, Zhang et al.[18] developed a pendulum-assisted multilayer structure, where stacked layers of fluorinated ethylene propylene (FEP) and copper where contacted due to the one-axis motion of the pendulum. They achieved a high power density of 200 Wm^{-3} on a see-saw testing system under 20° rotation amplitude. Tan et al.[23] developed a symmetric TENG capable of maintaining its operation after being overturned by waves. The device used a steel bar with a polytetrafluoroethylene (PTFE) coating rolling over an elliptical shaped Nylon film, which also acted upon other triboelectric pairs placed around the ellipse. They achieved powers of 90 μW at a frequency of 1 Hz and oscillation of amplitude 63°. Liang et al.[32] developed a multi-directional harvesting TENG, where a copper sphere acted upon spring-assisted stacked layers of copper and FEP. The device was optimized for 1 Hz waves, under which it achieved a power density of 4.81 Wm^{-3}. Rodrigues et al.[28] developed three different rolling-sphere TENGs, where stainless steel spheres contacted the triboelectric pairs of PTFE and Nylon. They considered realistic sea conditions, having tested the devices in a one-axis rotation system for wave periods from 1.5 to 7 s. Then, the devices were demonstrated to work successfully in a wave basin, with wave periods from 0.7 to 3.5 s.

In reality, a variety of testing conditions have been reported, tailored to better demonstrate the capabilities of each device and according to the type of moving element used. Nevertheless, a complete description on how sea states (wave period and amplitude) influence the moving element and the TENGs

I. Gonçalves, C. Rodrigues, J. Ventura
IFIMUP and Department of Physics and Astronomy
Faculty of Sciences
University of Porto
Rua do Campo Alegre 687, 4169-007 Porto, Portugal
E-mail: isabel.pintogoncalves@iit.it; joventur@fc.up.pt

The ORCID identification number(s) for the author(s) of this article can be found under https://doi.org/10.1002/aenm.202302627

DOI: 10.1002/aenm.202302627

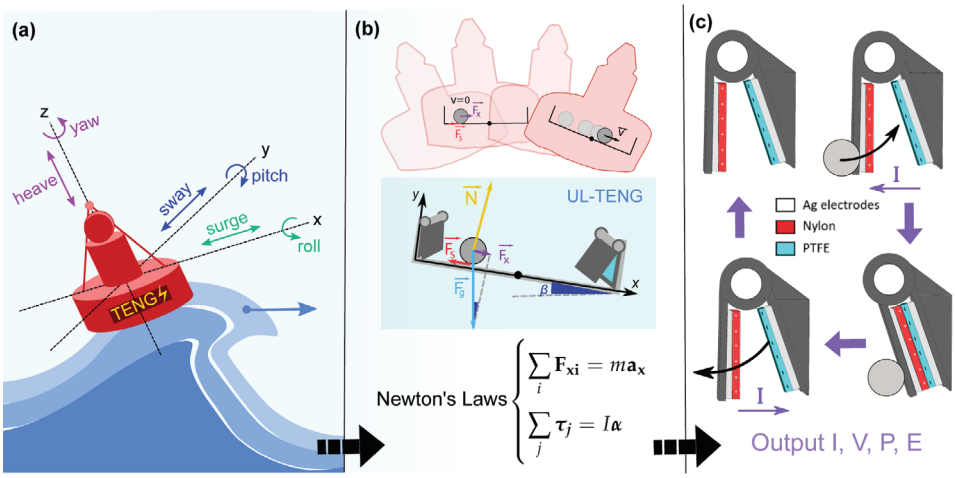

Figure 1. a) Axis of motion of an ocean buoy. b) Relevant forces acting on the device due to the buoy oscillation around the y-axis (pitch), where β is the pitch angle. c) Representation of the operation of our device. The mobile part is closed by a metallic sphere, making current flow through the external circuit in one direction. When the mobile part opens, current flows in the opposite direction.

output has so far been largely overlooked. One must evaluate the TENG performance considering that its optimum structure depends on the sea state of operation. This is often demonstrated by a resonant operation close to the natural frequency of the device.[22,28,35–37] Furthermore, the hydrodynamics of the encapsulation body should be taken into account.[28,38,39] A floating body, such as a buoy (**Figure 1**), is subjected to three axis of rotation (roll, pitch and yaw) and translation (surge, sway and heave).[14,40] Therefore, the motion dynamic is not imposed by the shape of the TENG, but rather by the encapsulation body. Finally, one should consider that, for prototyping purposes, the testing conditions (wave period and height) must be scaled down according to the size of the encapsulation body to obtain transferable results. For interactions between fluids and floating bodies, scaling relies on the Froude number similitude law, that states the similarity of inertial and gravitational forces between prototype and real scale model.[41] Therefore, the prototype and ocean buoys must have the same Froude number (Fr), given by[41–43]:

$$Fr = \frac{u}{\sqrt{gL}} \tag{1}$$

where u is the flow velocity, g is the local external field (gravity) and L is a characteristic length. This condition defines the scaling factors for wave periods and heights to be used in TENG prototyping. For all these reasons, a detailed understanding on how wave characteristics translate to the power generated in the final object to be deployed is critical for the successful application of TENGs in Blue Energy harvesting.

To describe and optimize TENG devices relying on moving bodies, we developed the unidirectional-lateral TENG (UL-TENG).[28] The UL-TENG is tailored to harvest the pitch rotation of a buoy, as depicted in Figure 1a. This rotation is characterized by the period T and angular amplitude of rotation (pitch value). As sketched in Figure 1b, the UL-TENG is composed of a linear track fixed to the buoy, two generators placed in opposite ends and a metallic sphere. Each generator is constituted by a structure fixed to the track and a mobile part that opens and closes freely. In the surface of the fixed structure there is a Ag/PTFE bilayer, while the mobile part has Ag/Nylon layers. As the track tilts, the sphere rolls down the tilted plane, accelerating toward and colliding with the nanogenerator, making the Nylon and PTFE layers come into contact (dielectric-dielectric mode) (Figure 1c). The kinetic energy of the sphere is then transferred to the generator, that converts it into electrical energy.

The introduction of a moving body adds a new twist to the system. In fact, the fascinating quality of the UL-TENG is the decoupling of the wave period, captured by the sphere, from the energy generation period, enclosed in the motion of the mobile part. In other words, the wave motion is not reproduced directly by the TENG, providing an advantageous tuning parameter. It is therefore necessary to understand how the sphere motion affects the energy generation mechanism. This can be achieved through careful modeling and experimental characterization of the device. To this end, the device was studied through numerical and analytical methods meant to replicate the sea conditions. In parallel, the device was characterized in a one-axis rotation system for a set of wave periods, pitch amplitudes and track lengths.

We observe that the velocity of our moving element is the link between wave characteristics and energy generation. Our analytical model of the sphere motion calculates the velocities of the sphere impact and of the contacting triboelectric layers for different wave parameters. Thanks to the momentum transfer of the sphere to the mobile part of each generator, the contact velocity is enhanced relative to the velocity of the sphere. Then, multiphysics modeling demonstrates a clear proportionality between the velocity of the contacting layers and the maximum power generated. Finally, the power output of our device shows a similar dependence on wave parameters as the sphere impact velocity. Thus, intentionally tuning the contacting layers velocity, in this case through a moving element decoupled from the generators, opens new paths for the design and optimization of TENGs.

2. Device Simulation

2.1. Analytical Model of Sphere Motion

As seen in Figure 1b, gravitational and static friction forces govern the motion of the moving element, here assumed to be 1D. The static friction ensures that the sphere is rolling without slipping at all times, while the dynamic friction was considered negligible. While both gravitational and static friction forces rule the linear motion of the sphere, the angular motion is provided by the static friction torque. Hence, one must solve Newton's laws for both linear and angular motions:

$$\begin{cases} \sum_i \mathbf{F}_{x_i} = m\mathbf{a}_x \\ \sum_j \boldsymbol{\tau}_j = I\boldsymbol{\alpha} \end{cases} \tag{2}$$

where m stands for the mass of the sphere, $I = \frac{2}{5}mR^2$ is its moment of inertia, R the radius, F_{x_i} any applied force along the x-axis, τ_j any applied torques, a_x the linear acceleration and α the angular acceleration. The resultant force acting on the sphere along the x-axis is the sum of the projected gravitational force, $F_x = mg\sin(\beta)$ and the static friction F_s:

$$m\frac{d^2x(t)}{dt^2} = F_x(t) - F_s(t) \tag{3}$$

The sphere then describes a linear motion along a tilted plane, in which the tilt angle $\beta(t)$ changes explicitly with time (t) as the track rotates according to the wave parameters. In one period, for a pitch amplitude A, β will change from -A (track rotates to the left) to A (track rotates to the right) back to -A. This results in a triangular function in time, with period equal to the wave period and amplitude equal to the wave pitch.

The sphere was considered to be initially at the highest position of the tilted track and rolling clockwise. The static friction is calculated from the torque as $\tau = \alpha I = -RF_s$ and, using $\alpha = -a_x R$, one obtains $F_s = F_x(\frac{I}{I+mR^2})$. Using the equation of linear motion [Equation (3)], one finally determines the system of equations to be solved:

$$\begin{cases} \frac{dv(t)}{dt} &= \frac{5}{7}g\sin[\beta(t)] \\ \frac{dx(t)}{dt} &= v(t) \end{cases} \tag{4}$$

2.2. Electrical Model of the UL-TENG

The capacitive model was used to compute not only the I (current), V (voltage) and P (power) characteristics of the TENG device, but also the generated energy for a fixed time interval. Our device was first modeled as a regular contact-separation TENG. This includes the assumptions that the triboelectric layers and electrodes are parallel (as the angle between them is <5°) and that the distance between the electrodes is much smaller than their lateral dimensions.

The instantaneous power provided at the load Z at which a TENG is connected is[8]:

$$P(t) = ZS\left\{\frac{\partial\sigma_I[z(t)]}{\partial t}\right\}^2 \tag{5}$$

where S is the surface area of the electrodes and σ_I is the induced charge that varies in time according to the relative position of the upper and bottom layers (air gap), $z(t)$.

The function $z(t)$ was defined as a triangular function with slope $\frac{dz(t)}{dt}$ equal to the velocity of the mobile part. To correlate the results with the period and pitch, this velocity was calculated from the collision of the sphere with the mobile part of the generator. The sphere velocity values just before impact were taken from the sphere motion simulation, and conservation of momentum was applied to convert it to the initial velocity of the mobile part of the generator. The collision was taken to be perfectly inelastic and 1D.

Then, σ_I was determined from the electric field integral over a path connecting the two electrodes, for each position of the TENG layers:

$$V = -\int \mathbf{E}\cdot\mathbf{dz} = ZS\frac{\partial\sigma_I[z(t)]}{\partial t} \tag{6}$$

where E is the electric field created by four infinite planes of charge, i.e. the two triboelectric layers and the two electrodes. Hence, for the contact-separation mode, the electric potential between electrodes becomes[7]:

$$V = \sigma_I\left(\frac{d_1}{\epsilon_1} + \frac{d_2}{\epsilon_2}\right) + (\sigma_I - \sigma_s)\frac{z}{\epsilon_0} \tag{7}$$

where d_1, d_2 are the thicknesses of the dielectrics, and ϵ_1, ϵ_2 their relative permittivities. In fact, Equation (7) is equivalent to the $V - Q - z$ relationship ($Q = S\sigma_I$) described by the capacitive model. Replacing Equation (7) in Equation (6), one can write:

$$ZS\frac{d\sigma_I(t)}{dt} - \sigma_I(t)\left(\frac{d_1}{\epsilon_1} + \frac{d_2}{\epsilon_2} + \frac{z}{\epsilon_0}\right) = \sigma_s\frac{z}{\epsilon_0} \tag{8}$$

This equation for $\sigma_I(t)$, together with Equation (5), completes our electrical model.

2.3. Multiphysics Model

In reality, the motion of the mobile part is better described as a rotation around the joint that connects the fixed and mobile parts, instead of a simple one axis contact-separation. Furthermore, the UL-TENG has finite, non-parallel contacting layers, so that its electrical outputs, in terms of I, V, and P, were also evaluated from finite element simulations with COMSOL Multiphysics. The geometry with angled layers is depicted in Figure S1a,b (Supporting Information). According to the electric potential distribution in space due to the triboelectric charges, the finite element software calculates the induced charge on the electrodes. The impact velocity of the sphere was converted to the contact velocity of the triboelectric layers, as described in Section 2.2. Then, each contact velocity value was taken as input for the motion of the generator in the COMSOL model. This way, the new position of all layers is computed, as stated by the analytically prescribed motion for a specific value of contact velocity. To achieve a new electrostatic equilibrium for the new configuration, the value of the induced charge on the electrodes is updated, taking into account the load resistance from

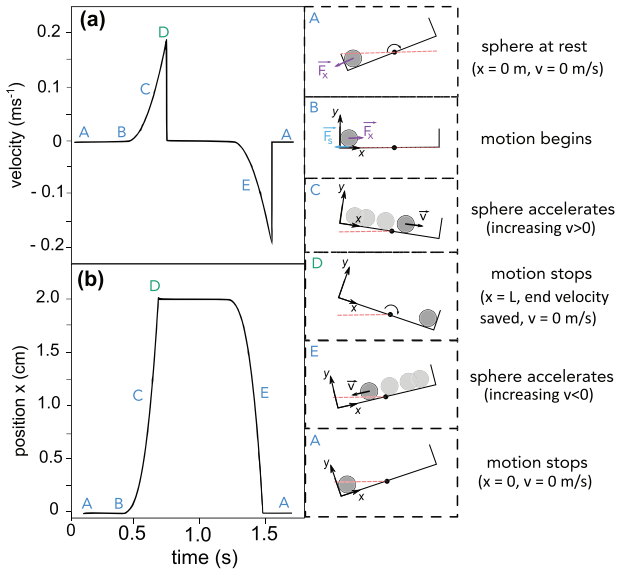

Figure 2. Left panel: a) Velocity profile for 2 cm track, period 1.57 s and pitch 20°. b) Corresponding position profile. Right panel: different phases of the forces acting on the sphere, its velocity and position, over one track rotation cycle. In position (D) the value of the velocity is recorded.

one electrode to the other. From the variation of the induced charge and the time step, the current through the resistance is calculated.

2.4. Numerical Results and Discussion

The simulated results for the position and velocity of the sphere for an illustrative period of 1.57 s, pitch of 20º ($-20° \leqslant \beta \leqslant 20°$) and track length of 2 cm are plotted in **Figure** 2a,b, respectively. The non-constant acceleration leads to the velocity profile depicted in Figure 2a, increasing non-linearly (C) up to a maximum value (D). This value corresponds to the impact velocity of the moving element, where the maximum position (2 cm) is reached. At this point, we determine the impact velocity (0.21 ms^{-1}) for the simulated wave and TENG parameters (period, pitch and track length). Then, the velocity is set to zero to account for the inelastic collision with the mobile part of the generator. While the track rotates toward the horizontal position, the sphere is still at rest, and only accelerates when β is high enough (E), until it reaches again the position x = 0 where the velocity is again set to zero (A).

According to the impact velocity saved in point D of Figure 2a, the *I-V-P* characteristics of the generator were determined from the COMSOL model. The electric potential distribution is calculated at each position of the generator, as depicted in **Figure** 3a for the fully opened (I) and the fully closed positions at 1 kΩ (II) and 100 MΩ (III). For the lower resistance, when the Nylon layer approaches the PTFE layer, the electric potential distribution in space is modified and current flows freely to account for that modification (peak current) (Figure 3c). When the generator is fully closed, there is a complete screening of the triboelectric charges and the current is zero (II). On the other hand, for a 100 MΩ resistance, the charges on the electrodes are almost immobile over the contact/separating cycle, and neutralization is very difficult to occur (Figure 3d). The resistances 1 kΩ and 100 MΩ were chosen to represent the short circuit and near open circuit values, respectively. As the current at low resistances suffered a negligible change (<1.5%) from 10 Ω to 1 kΩ, and the computing time is substantially increased for lower resistances, we refer to the latter for the short circuit condition. On the other hand, the higher the resistance, the longer the transient regime of the simulation, extending the final simulation time significantly. Since 100 MΩ is a resistance value orders of magnitude higher than the optimum resistance, we attribute this value to the open circuit condition. Nevertheless, as these terms could be misleading, we use "near open circuit voltage" to refer to the voltage at 100 MΩ.

As the contact velocity increases, the short circuit current also increases linearly (Figure 3e,h), as predicted by the capacitive model.[44] On the other hand, no major variations are observed on the near open circuit voltage value (Figure 3f,i; note the scale). For the highest velocities considered ($\geqslant 2$ ms^{-1}), the voltage reaches a stable value, indicating that the charges have become immobile. In fact, in near open circuit the charge flow is so slow that the electrodes cannot fully charge and discharge over the period of one cycle.[45] With the increase of the velocity of the contacting layers, the period of opening/closing the generator is shorter, which limits the charge and discharge processes even at smaller resistances. This indicates that the open circuit condition is reached for smaller load resistances when the velocity is higher. However, it is not attained for the lowest velocities ($\leqslant 1.5$ ms^{-1}), explaining the slightly upward trend with velocity for resistances 10 to 100 MΩ in Figure 3f. This leads to a shift in the optimum resistance from ≈ 1 MΩ to 30 kΩ, which is also consistent with the capacitive model.[44]

Finally, the power, for all resistances, increases with velocity as seen in Figure 3g,j. Moreover, the maximum power (at the optimum resistance) has a linear dependence on contact velocity. These results point to a direct and significant influence of the impact velocity on the electrical output of our device. The influence of velocity in *I–V–P* characteristics was validated by comparison with the capacitive model, as described in Figure S1c–e (Supporting Information).

3. Results and Discussion

Given the presence of two generators at each end of the track, we started by studying how the electrical connection between them influences the obtained current and voltage. We observe that the anti-parallel connection provides the highest I_{SC} and V_{OC} (**Figure** 4a,b), slightly better than the parallel connection. This was further confirmed averaging both positive and negative current and voltage peaks. These tests were performed at 15° pitch and 2 s period. This improvement can be understood from the connection diagrams in Figure 4a,b. The generators are in antiphase, i.e., when one is closed by the sphere, the other opens. If they are connected in parallel (inset in Figure 4a) they generate currents in opposite directions, or equivalently, when the output peak of one generator is positive, the other will be negative. On the other hand, the anti-parallel connection (inset in Figure 4b) ensures that the current from each generator adds, reinforcing the total electrical signal transferred to the load resistance.

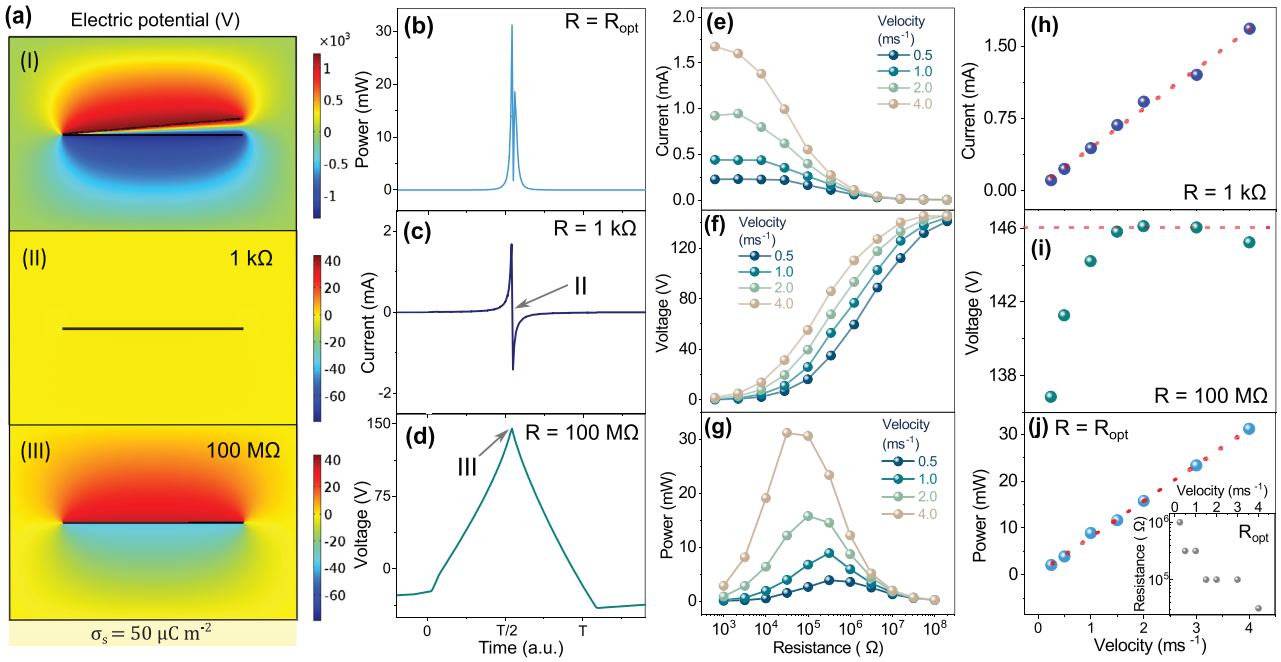

Figure 3. a) Electric potential distribution calculated by COMSOL Multiphysics for (I) initial conditions and closed generator at (II) 1 kΩ and (III) 100 MΩ. b) Power, c) current and d) voltage peaks at different resistances. e) Current, f) voltage, and g) power characteristic curves as simulated in COMSOL Multiphysics. h) Short circuit current and i) near open circuit voltage and j) maximum power, with inset showing the optimum resistance, for different contact velocities.

Furthermore, it was observed that the optimum resistance varies with the period and pitch (Figure 4c), as predicted by the presented multiphysics simulations, being smaller for higher contact velocities. This is here exemplified for (period, pitch) pairs of (1 s, 45°) and (3 s, 15°), with the first pair experimentally showing smaller optimum resistance and higher contact velocity (see also **Figure 5b**).

The observed voltage peaks (Figure 4d–k) depend on the period and pitch of the rotational motion and the track length, i.e., the maximum travelling length of the sphere. A clear observation is that, for each track and period, the voltage peaks are steadily enhanced by the increase of pitch from 5° to 45° (Figure 4d–g). A larger tilt means the sphere will accelerate faster and impact the nanogenerator with a higher velocity, producing a higher output. In some particular cases a periodic output is absent, for instance, for a pitch of 5°, period 1 s and track lengths of 10 and 15 cm (Figure 4h). This occurs because the track is too long for the sphere to reach the nanogenerators on both ends, so it oscillates around the center of the track. In other occasions, the sphere can become trapped in one of the extremities, activating only one generator, hence producing the response shown in Figure 4h, for 20 cm. For a pitch of 15° and period of 1 s (Figure 4i), the optimum track length is 15 cm, as assessed from the average of positive and negative voltage and current peaks, since for the other lengths this output is reduced. This is due to the asynchronous motion of the sphere with the track. When the sphere does not reach the generators with the maximum velocity possible for that track length, the output is sub-optimal, and other track lengths are ideal at harvesting that motion, i.e., that specific period and pitch.

3.1. Wave Parameters Influence on TENG Performance

The data obtained for different wave parameters is presented in Figure 5, along with results from our model, in order to immediately compare them. Under different wave periods and pitches, the power generated by the UL-TENG changes significantly, as shown in Figure 5a. The maximum power is always obtained at the maximum pitch of 45° and smallest period of 1 s. These correspond to wave parameters for which the sphere is highly accelerated. As the track length increases from 5 to 20 cm, the maximum power obtained also increases from 192 to 381 μ*W*, with the maximum power density of 1.9 Wm^{-3} obtained for a 20 cm track, period of 1 s and pitch of 45°. Moreover, the region of high power tends to move toward larger periods, i.e., longer tracks will optimally harvest waves of longer periods. However, smaller periods are better harvested with the 5 cm track.

These results are coherent with the sphere velocity simulations presented in Figure 5b. The maximum velocity value also increases with track length, since the sphere accelerates over longer distances. Coincidentally, the region of high velocity is also located on the smallest periods, highest pitch corner of the map, and moves upward toward longer periods as the track gets longer. Meanwhile, for 15 and 20 cm, there is an area of zero velocity, that corresponds to the cases where the sphere oscillates around the center of the track, without touching the generators.

As seen from the previous discussion, pitch is identified as the determinant parameter maximizing the output. Higher waves will produce larger oscillations and hence the sphere will reach a higher velocity before impact, yielding a higher power. On the

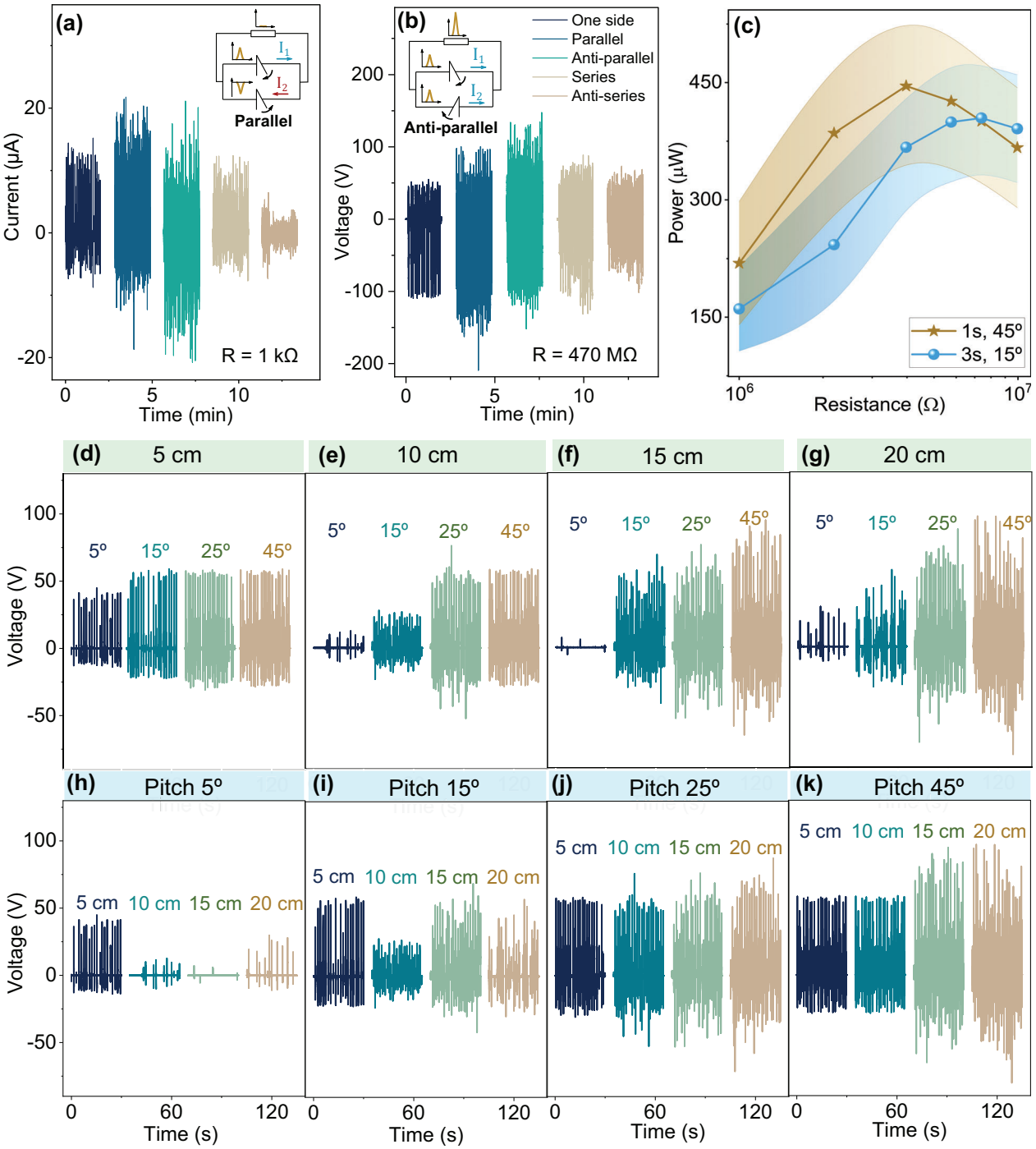

Figure 4. a) Short circuit current and b) open circuit voltage for different types of connection of the two generators. c) Peak power for two states of different impact velocity. TENG voltage output for different pitches and track lengths d) 5 cm, e) 10 cm, f) 15 cm, g) 20 cm. TENG voltage output for different track lengths, and pitches h) 5°, i) 15°, j) 25°, k) 45°, for 1 s period of motion.

other hand, the period becomes important when considering the track length, since this will affect the synchrony between the sphere motion and the tilting of the track. Ideally, the acceleration increases with time as the track tilts and the sphere rolls down. However, in some cases, if the tracks start rotating up when the sphere is still rolling down the slope, the sphere will not reach the nanogenerator at its maximum acceleration, resulting in a sub-optimal impact velocity.

In the ocean, TENGs will be providing power to charge either a capacitor or battery. In this situation, the wave period will define the frequency of the energy transferring events. Hence, just as the instantaneous power, the energy transferred in a certain

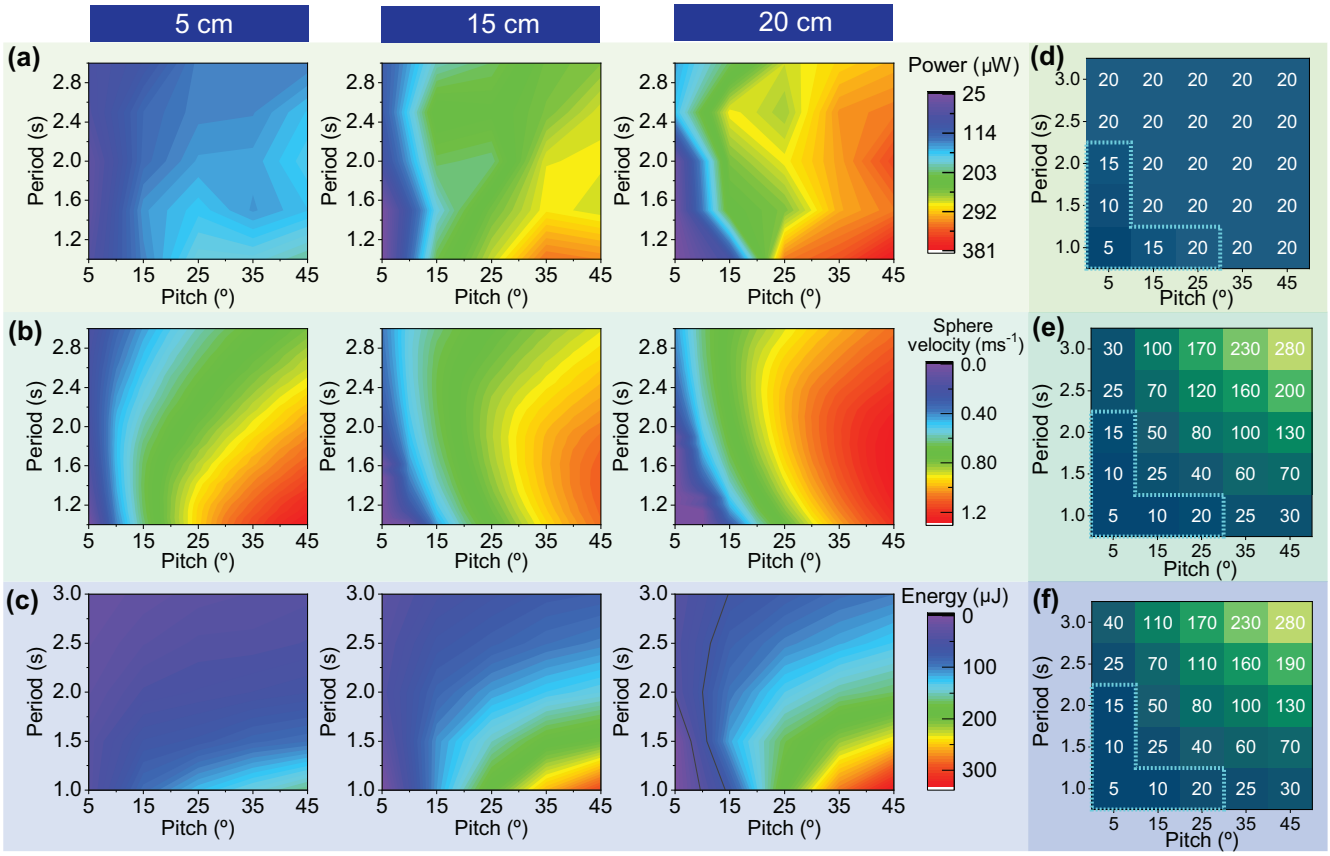

Figure 5. 2D map of a) measured power, b) simulated sphere impact velocity and c) simulated energy over 60 s, as function of the motion parameters period and pitch. Optimum track length (in cm) to harvest specific periods and pitches according to d) measured power, e) simulated impact velocity and f) simulated energy over 60 s.

period of time becomes relevant. To understand if more frequent, moderately intense peaks of power could result in a larger harvested energy than less frequent, higher power peaks, the energy harvested in 60 s was calculated. In fact, an additional favorable factor for energy transfer in this kind of devices is the larger mass of the sphere relative to the mobile part of the generator. While the impact velocities were in the [0, 1.3] ms^{-1} range, the layers contact velocity reached 4 ms^{-1}, a more than twofold increase than can be further explored by tuning the masses. As expected, the wave period becomes much more important, as seen in Figure 5c. As the track length increases, the region of high energy is much more confined, and the maximum value changes from 161 μJ at 5 cm to 333 μJ at 20 cm. This means there is a trade-off between peak power and time between peaks, where high power, long period operation (for instance, for 45° and 3 s), yields similar energy to low power, medium period operation (15° and 1.5 s).

3.2. Optimized Design Determination

Device optimizing implies determining the combination of pitch, period and track length that leads to a synchronous operation with the largest oscillation possible. This can be achieved by tuning the track length for each pair of period and pitch. We evaluated the optimum track length, from the admitted possible values of 5 cm to 3 m (with discretization of 5 cm) for all pairs of wave parameters considered. The first map in Figure 5d considers as criterion the power measured experimentally, the second the final velocity, and the third the generated energy in 60 s. Since only 5, 10, 15, and 20 cm tracks were measured experimentally, the power map (Figure 5e) is limited to these lengths. On the other hand, as obtained numerically, the track lengths that maximize impact velocity and energy spread up to 2.8 m. However, considering only tracks up to 20 cm, there is an almost full agreement on the experimental and simulated optimum track lengths, as can be seen comparing the maps in Figure 5d,e, showing power and velocity maximization, respectively.

Considering the optimum track length for optimized energy harvesting in 60 s, surprisingly there is also a consensus for most of the map (Figure 5f), comparing to the previous two (Figure 5d,e). This shows that the effect of larger waiting time in between power peaks (in the case of longer periods) is the same for all track lengths, so that, overall, the optimum track length for each pair of period and pitch remains unaffected. The disagreement between the velocity and energy maps (Figure 5e,f) occurs for periods larger than 2 s, for instance, for the (period, pitch) pairs of (5°, 3 s) and (45°, 2.5 s), where this reasoning might start to break. As the interval between peaks increases, there is a significant reduction in the energy produced over 60 s, as seen on

Figure 5c. Therefore, with larger waiting times between peaks, power is less frequently transferred to the load, which means that the best track length for that (period, pitch) pair that optimizes energy production is now different from the one that optimizes power.

The identification of the same optimum track length, for each period and pitch, that yields the maximum impact velocity and the maximum TENG power reveals that velocity is the critical parameter on which the TENG power depends. Furthermore, the optimization based on track length poses an advantage from a design point of view, since it will allow to tailor TENGs to specific sea states. In addition, different TENGs, with different track lengths, can be stacked to increase the range of optimized harvesting in the period and pitch space.

4. Conclusion

In this work, a correlation between the motion of a Blue Energy TENG and its electrical output was established. This comprised both the numerical and analytical modeling of the device plus experimental characterization, since simulations provided a valuable insight on the understanding of the experimental results. First, the current and voltage peak shapes were better understood at the light of COMSOL Multiphysics simulations, that provided a correspondence between the position of the layers and the evolution of a current/voltage peak. Second, the deviation of the optimum resistance observed experimentally for different periods and pitches was connected to the different contact velocities of the triboelectric layers as predicted by the device simulation. Third, the generated energy was predicted to critically depend on the wave period, and close attention must be paid in the future when considering long periods relative to the total observation time.

Finally, the velocity of the moving element proved to be a crucial parameter on the generated power of our device. By making different the time to contact the triboelectric layers from the wave period, we were able to enhance the velocity of the contacting layers due to momentum transfer from a moving element, improving the power output. This was shown by numerical simulations and later supported by the similar dependence on wave period and pitch of both the obtained power (experimental) and velocity of the sphere (simulated). This work elucidated the influence of the contacting layers velocity in the output of TENGs. While in our case, this velocity was imposed by the sphere velocity, these findings can be applied in any device (based on TENGs or other energy harvesting mechanism) relying on moving elements, specially those where the contact velocity can be tuned intentionally.

5. Experimental Section

Similitude Analysis: This study was based on a 1:8 scaled prototype, relative to a full scale Atlantic-2600 navigational buoy. From this results that the wave height was scaled down by a factor of 8 and the period by a factor of $\sqrt{8}$. Since the ocean buoy was typically subjected to wave periods and heights in [2.1, 10] s and [50, 200] cm intervals,[28] from Equation (1) results that the scaled down buoy would move according to wave periods and heights in [0.74, 3.5] s and [6.25, 25] cm ranges, respectively. For the track lengths considered of 5 to 20 cm, these wave heights correspond to pitch amplitudes in the [5, 45]° range.

Analytical and Electrical Models: The equations of motion of the sphere [Equation (4)] were solved with a fourth-order Runge Kutta (RK4) method in Python. Python was also used for the electrical model. Equation (8) was solved for the parameters of the device and $\sigma_s = 50\ \mu Cm^{-2}$ with RK4. The RK4 temporal step was adjusted according to the convergence for each resistance. The lower the resistance, the smaller the step size for the method to converge (used step sized ranged from 10^{-8} to 10^{-6} s). The power was calculated using Equation (5) with a regular differentiation algorithm. To obtain the energy produced in 60 s, the power peaks were integrated in time over a cycle and multiplied over the number of cycles.

COMSOL Settings: With the *Electrostatics* module, the triboelectric charge density was defined at the dielectrics surface (assumed saturated, $\sigma_s = 50\ \mu Cm^{-2}$) and a *Terminal* condition applied to the boundary between each dielectric and electrode. This allowed the connection of the electrodes to a resistor through an *External Coupling* called *External I versus U*, both belonging to the Electrical Circuit module. To complete the basic components of the model, there was the *Moving Mesh* module performing the *Prescribed Deformation* and *Prescribed Mesh Displacement* at the top dielectric/electrode layer, as well as attributing a *Free Deformation* to the air domain to accommodate for the changes in position and mesh of the moving layers. Appropriate boundary conditions, re-meshing during runtime, use of a nonlinear time dependent solver and total simulation time were chosen to yield meaningful results.

Experimental Methods: Each generator was fabricated by an easy and low cost procedure. Silver films were screen printed onto PTFE (50 μm thick) and Nylon (17 μm) films and dried for 20 min at 120°C in a heating chamber. The rotating and fixed part of the generators were 3D printed in black polylactic acid (PLA). The PTFE/Ag and Nylon 6,6/Ag films were attached to the PLA parts, with dimensions of $2.65 \times 3.75\ cm^2$. Each generator was then assembled onto a track of variable length. A servo motor controlled by Arduino exerts the rotation of the metallic frame where the track is fixed. All electrical quantities were acquired with a Keithley 6514 Electrometer. The TENG was connected to an electronic switching board, that programatically changes between series or parallel configuration to acquire current and voltage, respectively. Different resistances were provided by another switchable circuit board, from 100 Ω to 470 MΩ. Individual resistances in the range of 1 to 10 MΩ were used to evaluate the variation of the optimum resistance with velocity. Finally, the acquisition and motion were synchronized and integrated in one main Labview user interface, allowing the system to collect hours of data autonomously. To study the dependence of the output on period and pitch, the electrical power was obtained from voltage and current measurements averaged over 40 cycles, with peaks representatively selected from a standard normal distribution.

Supporting Information

Supporting Information is available from the Wiley Online Library or from the author.

Acknowledgements

The authors acknowledge funding from project 2022.05030.PTDC from FCT. FSE/POPH, FEDER, COMPETE and ON2 are also acknowledged. The authors also acknowledge support from the International Consortium of Nanotechnologies (ICON) funded by Lloyd's Register Foundation, a charitable foundation that helps to protect life and property by supporting engineering-related education, public engagement and the application of research. C.R. is thankful to FCT for grant SFRH/BD/147811/2019.

Conflict of Interest

The authors declare no conflict of interest.

Data Availability Statement

The data that support the findings of this study are available from the corresponding author upon reasonable request.

Keywords

motion dynamics, multiphysics modelling, ocean waves energy harvesting, optimization of TENGs output, tailored harvesting of sea states, triboelectric nanogenerators

Received: August 10, 2023
Revised: October 5, 2023
Published online: November 23, 2023

[1] World Meteorological Organization, State of the global climate 2022, Tech. rep. WMO, **2022**, https://library.wmo.int/records/item/66214-state-of-the-global-climate-2022.
[2] International Energy Agency, World Energy Outlook 2022. In: *IEA* **2022**. ISSN: CC BY 4.0 (report); CC BY NC SA 4.0 (Annex A).
[3] M. K. Hoffacker, R. R. Hernandez, *Front. Sustain.* **2020**, *1*, 585110.
[4] F. Taveira-Pinto, G. Iglesias, P. Rosa-Santos, Z. D. Deng, *J. Renewable Sustainable Energy* **2015**, *7*, 6.
[5] A. Lewis, S. Estefen, J. Huckerby, K. S. Lee, W. Musial, T. Pontes, J. Torres-Martinez, D. Bharathan, H. Hanson, G. Heath, et al., in *Renewable Energy Sources and Climate Change Mitigation: Special Report of the Intergovernmental Panel on Climate Change* (Eds: O. Edenhofer, et al.), Cambridge University Press, Cambridge, **2011**, pp. 497–534.
[6] Our World in Data, Global direct primary energy consumption, **2023**, https://ourworldindata.org/grapher/global-primary-energy, (accessed: May 2023).
[7] Z. L. Wang, T. Jiang, L. Xu, *Nano Energy* **2017**, *39*, 9.
[8] Z. L. Wang, *Nano Energy* **2020**, *68*, 104272.
[9] X. Yang, S. Chan, L. Wang, W. A. Daoud, *Nano Energy* **2018**, *44*, 388.
[10] C. Zhang, Y. Hao, J. Yang, W. Su, H. Zhang, J. Wang, Z. L. Wang, X. Li, *Adv. Energy Mater.* **2023**, *13*, 2300387.
[11] S. Niu, Z. L. Wang, *Nano Energy* **2015**, *14*, 161.
[12] Z. L. Wang, *Mater. Today* **2017**, *20*, 74.
[13] Z. Ren, X. Liang, D. Liu, X. Li, J. Ping, Z. Wang, Z. L. Wang, *Adv. Energy Mater.* **2021**, *11*, 2101116.
[14] C. Rodrigues, D. Nunes, D. Clemente, N. Mathias, J. M. Correia, P. Rosa-Santos, F. Taveira-Pinto, T. Morais, A. Pereira, J. Ventura, *Energy Environ. Sci.* **2020**, *13*, 2657.
[15] H. Wang, C. Zhu, W. Wang, R. Xu, M. Xu, *Nanomaterials* **2022**, *12*, 594.
[16] X. Chen, L. Gao, J. Chen, S. Lu, H. Zhou, T. Wang, A. Wang, Z. Zhang, S. Guo, X. Mu, Z. L. Wang, Y. Yang, *Nano Energy* **2020**, *69*, 104440.
[17] C. Hou, T. Chen, Y. Li, M. Huang, Q. Shi, H. Liu, L. Sun, C. Lee, *Nano Energy* **2019**, *63*, 103871.
[18] C. Zhang, L. Zhou, P. Cheng, D. Liu, C. Zhang, X. Li, S. Li, J. Wang, Z. L. Wang, *Adv. Energy Mater.* **2021**, *11*, 2003616.
[19] W. Zhong, L. Xu, H. Wang, D. Li, Z. L. Wang, *Nano Energy* **2019**, *66*, 104108.
[20] F. Zheng, Y. Sun, X. Wei, J. Chen, Z. Yuan, X. Jin, L. Tao, Z. Wu, *Nano Energy* **2021**, *90*, 106631.
[21] Z. Lin, B. Zhang, H. Guo, Z. Wu, H. Zou, J. Yang, Z. L. Wang, *Nano Energy* **2019**, *64*, 103908.
[22] C. Zhang, L. He, L. Zhou, O. Yang, W. Yuan, X. Wei, Y. Liu, L. Lu, J. Wang, Z. L. Wang, *Joule* **2021**, *5*, 1613.
[23] D. Tan, Q. Zeng, X. Wang, S. Yuan, Y. Luo, X. Zhang, L. Tan, C. Hu, G. Liu, *Nano-Micro Lett.* **2022**, *14*, 1.
[24] D. Y. Kim, H. S. Kim, D. S. Kong, M. Choi, H. B. Kim, J.-H. Lee, G. Murillo, M. Lee, S. S. Kim, J. H. Jung, *Nano Energy* **2018**, *45*, 247.
[25] H. Yang, W. Liu, Y. Xi, M. Lai, H. Guo, G. Liu, M. Wang, T. Li, X. Ji, X. Li, *Nano Energy* **2018**, *47*, 539.
[26] P. Cheng, H. Guo, Z. Wen, C. Zhang, X. Yin, X. Li, D. Liu, W. Song, X. Sun, J. Wang, Z. L. Wang, *Nano Energy* **2019**, *57*, 432.
[27] M. Xu, T. Zhao, C. Wang, S. L. Zhang, Z. Li, X. Pan, Z. L. Wang, *ACS Nano* **2019**, *13*, 1932.
[28] C. Rodrigues, M. Ramos, R. Esteves, J. Correia, D. Clemente, F. Gonçalves, N. Mathias, M. Gomes, J. Silva, C. Duarte, T. Morais, P. Rosa-Santos, F. Taveira-Pinto, A. Pereira, J. Ventura, *Nano Energy* **2021**, *84*, 105890.
[29] X. Yang, L. Xu, P. Lin, W. Zhong, Y. Bai, J. Luo, J. Chen, Z. L. Wang, *Nano Energy* **2019**, *60*, 404.
[30] H. Wang, Z. Fan, T. Zhao, J. Dong, S. Wang, Y. Wang, X. Xiao, C. Liu, X. Pan, Y. Zhao, M. Xu, *Nano Energy* **2021**, *84*, 105920.
[31] L. Liu, X. Yang, L. Zhao, H. Hong, H. Cui, J. Duan, Q. Yang, Q. Tang, *ACS Nano* **2021**, *15*, 9412.
[32] X. Liang, T. Jiang, G. Liu, Y. Feng, C. Zhang, Z. L. Wang, *Energy Environ. Sci.* **2020**, *13*, 277.
[33] Y. Wang, A. M. Nazar, J. Wang, K. Xia, P. Jiao, *J. Marine Sci. Eng.* **2022**, *10*, 5.
[34] A. Ahmed, Z. Saadatnia, I. Hassan, Y. Zi, Y. Xi, X. He, J. Zu, Z. L. Wang, *Adv. Energy Mater.* **2017**, *7*, 1601705.
[35] M. Xu, P. Wang, Y.-C. Wang, S. L. Zhang, Z. L. Wang, *Adv. Energy Mater.* **2017**, *8*, 9.
[36] X. Wang, S. Niu, Y. Yin, F. Yi, Z. You, Z. L. Wang, *Adv. Energy Mater.* **2015**, *5*, 1501467.
[37] T. Jiang, H. Pang, J. An, P. Lu, Y. Feng, X. Liang, W. Zhong, Z. L. Wang, *Adv. Energy Mater.* **2020**, *10*, 2000064.
[38] C. Jin, H. Kang, M. Kim, I. Cho, *Renewable Energy* **2020**, *160*, 2000064.
[39] A. F. de O. Falcão, *Renewable Sustainable Energy Rev.* **2010**, *14*, 899.
[40] J. H. Todalshaug, in *Handbook of Ocean Wave Energy*, Springer, Cham, Switzerland **2016**, pp. 139–158.
[41] C. Ruzzo, S. Muggiasca, G. Malara, F. Taruffi, M. Belloli, M. Collu, L. Li, G. Brizzi, F. Arena, *Appl. Ocean Res.* **2021**, *108*, 102487.
[42] R. G. Coe, V. S. Neary, *in Proceedings of the Annual Marine Energy Technology Symposium (METS)*, Seattle, USA, **2014** (accessed: November 2023).
[43] C. Lin, M.-J. Kao, J. Yang, R. V. Raikar, S.-C. Hsieh, *Processes* **2021**, *9*, 1420.
[44] S. Niu, S. Wang, L. Lin, Y. Liu, Y. S. Zhou, Y. Hu, Z. L. Wang, *Energy Environ. Sci.* **2013**, *6*, 3576.
[45] C. Callaty, I. Gonçalves, C. Rodrigues, J. Ventura, *Curr. Appl. Phys.* **2023**, *50*, 100.